

# Benchmarking collective effects of electron interactions in a wiggler with OPAL-FEL <sup>☆</sup>

Arnau Albà <sup>a</sup>, Jimin Seok <sup>b,c</sup>, Andreas Adelmann <sup>a,\*</sup>, Scott Doran <sup>b</sup>, Gwanghui Ha <sup>b</sup>, Soonhong Lee <sup>b</sup>, Yinghu Piao <sup>b</sup>, John Power <sup>b</sup>, Maofei Qian <sup>b</sup>, Eric Wisniewski <sup>b</sup>, Joseph Xu <sup>b</sup>, Alexander Zholents <sup>b</sup>

<sup>a</sup> Paul Scherrer Institut, Villigen, 5232, Switzerland

<sup>b</sup> Argonne National Laboratory, Lemont, 60439, IL, USA

<sup>c</sup> Ulsan National Institute of Science and Technology, Ulsan, 44919, Gyeongnam, South Korea

## ARTICLE INFO

### Article history:

Received 8 December 2021

Received in revised form 4 July 2022

Accepted 24 July 2022

Available online 28 July 2022

### Keywords:

Accelerator physics

Wiggler

Radiation

Computational electromagnetics

Microbunching

Electron cooling

## ABSTRACT

OPAL-FEL is a recently developed tool for the modeling of particle accelerators containing wigglers or undulators. It extends the well established 3D electrostatic particle-tracking code OPAL, by merging it with the finite-difference time-domain electromagnetic solver MITHRA. We present results of two benchmark cases where OPAL-FEL simulations are compared to experimental results. Both experiments concern electron beamlines where the longitudinal phase space is modulated with a short magnetic wiggler. Good agreement was found in both the space charge and radiation dominated regimes.

© 2022 The Author(s). Published by Elsevier B.V. This is an open access article under the CC BY license (<http://creativecommons.org/licenses/by/4.0/>).

## 1. Introduction

Wiggler magnets, consisting of alternating polarity dipole magnets with a strong transverse magnetic field, are used in electron/positron storage rings as devices for producing intense synchrotron radiation. See [1–3] and references therein for an in depth introduction to wigglers and undulators and descriptions of their diverse applications. Coherent synchrotron radiation (CSR) in wiggler magnets can cause a microwave-like beam instability in storage rings as suggested in [4] and evidenced in [5]. The observations in [6–9] may also be associated with a CSR-driven instability. These findings inspired the study of the longitudinal wakefield and impedance effect in a wiggler due to CSR described in [10]. With the advent of the free-electron lasers (FELs), wigglers began to be employed in setups aiming for enhanced self-amplified spontaneous emission [11,12] and setups that explore the wiggler's CSR for electron microbunching and obtaining large and narrow peak current spikes [13]. These current spikes cause strong longitudinal space charge forces as discussed in [14] that are particularly

noticeable in the wiggler where the beam propagates with reduced average longitudinal velocity  $\bar{v}_z = c\sqrt{1 - 1/\gamma_z^2}$ , where  $c$  is the speed of light and  $\gamma_z = \gamma/\sqrt{1 + K^2/2}$ . Here  $\gamma$  is the relativistic factor and  $K = eB_w\lambda_w/2\pi mc^2$  is the wiggler parameter, where  $e, m$  are the electron charge and mass,  $\lambda_w$  is the wiggler's period, and  $B_w$  is the wiggler's peak magnetic field. When  $K^2 \gg 1$ , the wiggler strongly influences the longitudinal space charge force such that the frequency of plasma oscillations inside the electron bunch propagating through the wiggler become a factor of  $\gamma/\gamma_z$  larger than the frequency of the plasma oscillations in a drift section [15] and, thus, the wiggler can be conveniently used to control the plasma oscillation frequency. This feature can be useful for microbunched electron cooling (see, [16,17] and references therein), in which one can consider shortening the amplification cascades by replacing the drifts with wigglers. However, due to CSR, the evolution of the microbunched beam inside the wiggler is more complex than in the drift and must be analyzed considering simultaneously the radiation and space charge forces. To the best of our knowledge, this analysis can only be performed in the integral form [15,18] or numerically using a code based on first-principle equations.

Many computer tools for modeling wigglers and undulators have been developed during the last 20 years due to the increasing

<sup>☆</sup> The review of this paper was arranged by Prof. Z. Was.

\* Corresponding author.

E-mail address: [andreas.adelmann@psi.ch](mailto:andreas.adelmann@psi.ch) (A. Adelmann).

number of FEL facilities (some examples [19–21]). However, these codes often make assumptions to be computationally efficient at the cost of limiting their applicability to certain types of FELs (see [22] for a detailed comparison of FEL codes). For the experiments considered in this paper, it was necessary to use the less common electromagnetic particle-in-cell (EM-PIC) codes, which solve the full inhomogeneous Maxwell equations, and also simulate particles. Examples of such codes are OSIRIS [23] and MITHRA [22]. In this paper, we present and use OPAL-FEL [24], a combination of the 3D electrostatic code OPAL [25] and MITHRA. This code accounts for 3D effects and solves first-principle equations, making it very attractive for modeling the microbunched electron beam in a wiggler, but, it must first be benchmarked to experimental results. In this paper, we discuss the result of benchmarking simulations performed using OPAL-FEL for two experiments, one at SLAC using a wiggler and a high energy beam at LCLS in the regime dominated by CSR, and one at ANL using a wiggler and a low energy beam at AWA in the regime dominated by space charge.

## 2. OPAL-FEL

Having computational tools capable of accurately modeling accelerators has become essential for the study of complex phenomena in beam physics. The open source framework OPAL (Object Oriented Parallel Accelerator Library) [25] is a parallel, fully 3D code for the simulation of charged particle beams. To compute space charge forces within the bunch, OPAL simplifies Maxwell's equations using the static approximation, and solves them using particle-in-cell methods. While this approach is sufficient for many problems in accelerator science, it cannot account for the propagation of electromagnetic waves, since the coupling between electric and magnetic fields is lost due to the static approximation. OPAL simulations can therefore not include wigglers and undulators, where the particle-wave interactions cannot be neglected. Note that OPAL comes in two flavours, OPAL-cycl and OPAL-t, the latter of which is aimed at modeling straight beamlines, which is the focus of this work. Throughout the paper we will interchangeably use the terms OPAL and OPAL-t.

In order to model beamlines that do include wigglers, we recently added a new full-wave solver into OPAL. Rather than coding this solver from scratch, we wrote a wrapper that makes use of the external library MITHRA. MITHRA [22] is a full-wave simulation tool that models electron interactions in a wiggler starting from first principles. It was originally conceived as a standalone code for the simulation of undulators, but for this work we adapted it into a library that can be called from within OPAL. This new flavour of OPAL, OPAL-FEL, can switch back and forth between the static and the full-wave solver during the course of a simulation, such that beamline sections containing undulators or wigglers are correctly modeled and include radiation. In the following sections we explain in more detail how the static and full-wave solvers work, and the challenges of merging them in OPAL-FEL.

### 2.1. OPAL static solver

To compute self fields and space charge forces in the charged particle beam, OPAL's static solver solves the electrostatic Maxwell equations at each time step, which are

$$\begin{cases} \vec{\nabla} \cdot \vec{E} = \rho \\ \vec{\nabla} \cdot \vec{B} = \mu_0 \vec{j} \end{cases} \quad (1)$$

where  $\vec{E}$ ,  $\vec{B}$  are the electric and magnetic fields respectively,  $\vec{j}$  the current density, and  $\rho$  the charge density. In order to fulfil the electrostatic condition, a Lorentz transformation into a frame of reference moving at the bunch's average speed  $\beta$  is performed

before solving the equations, which means that the particles are quasi-static and the current and the resulting magnetic are small i.e.  $\vec{B} = \vec{j} \simeq 0$ . This leaves us with a single elliptic PDE to be solved in the comoving frame, Poisson's equation:

$$\nabla^2 \phi = -\frac{\rho}{\epsilon_0} \quad (2)$$

with adequate boundary conditions. Once the scalar potential  $\phi$  has been computed, it can be used to compute the electric field in the comoving frame  $\vec{E}$ , followed by a Lorentz transformation back into the laboratory frame that yields both magnetic and electric fields:

$$\begin{cases} \vec{E}_{lab} = \gamma \vec{E} - (\gamma - 1) E_z \hat{z}, \\ \vec{B}_{lab} = \gamma \frac{\vec{\beta} \wedge \vec{E}}{c}. \end{cases} \quad (3)$$

To solve Poisson's equation efficiently OPAL uses a particle-in-cell (PIC) scheme [26]. At each time step the charge density  $\rho$  is interpolated to a grid of points that surrounds the bunch. Note that this grid, which contains a fixed number of cells during the whole simulation, is stretched and rotated at each time step, such that it tightly encloses the entire bunch. The grid is then Lorentz boosted into the static frame, where Poisson's equation is solved, and then boosted back into the lab frame. Then, in the lab frame, the fields can be interpolated back from the grid to the particle positions. A solution to Poisson's equation is a convolution between the charge density  $\rho$  and the Green's function subject to the appropriate boundary conditions [26,25]. Finally the Boris pusher scheme [27] is used to update the positions and momenta of the particles. Fig. 1 schematically shows how the static solver works.

This solver is fully parallelized with MPI, using 3D domain decomposition and parallel FFTs. With this method we generally require many more particles than cells  $N_p \gg N_c$ , and therefore the solver performs constant load-balancing such that particles are evenly shared among processors.

### 2.2. OPAL-FEL full-wave solver

To the best of our knowledge, there are no open-source 3D particle-tracking codes that can model start-to-end beamlines that include undulators, using first-principle equations. Most 3D particle-tracking codes (e.g. [28,29]) use the electrostatic approximation, like OPAL. On the other hand, in the last twenty years so-called FEL codes have been developed with the specific goal of modeling undulators. These codes are aimed at simulating the bunch only as it goes through the undulator, rather than simulating a full beamline. Moreover, FEL codes in general do not solve Maxwell's equations from first principles, and instead make approximations that lead to less computationally expensive algorithms. A notable exception is MITHRA [22], a recently developed FEL code that models undulators starting from first-principles by solving Maxwell's equations in 3D. A full comparison of MITHRA with other FEL codes can be found in the original paper [22].

As mentioned at the beginning of this chapter, MITHRA was adapted into a library and integrated into OPAL-t as a solver. In addition to being able to model undulators and wigglers, MITHRA, like OPAL, is written in C++, is open-source, and uses MPI for parallelization, all reasons that contributed to making MITHRA a good candidate for being merged with OPAL.

OPAL's static solver cannot account for radiation effects, and it is for this reason that up until now OPAL could not include wiggler or undulators. Hence, modeling micro-bunching and coherent radiation in FEL was not possible. In order to fully capture the physics of an undulator one needs to compute the electromagnetic fields by solving the full Maxwell equations [30]. In the following lines

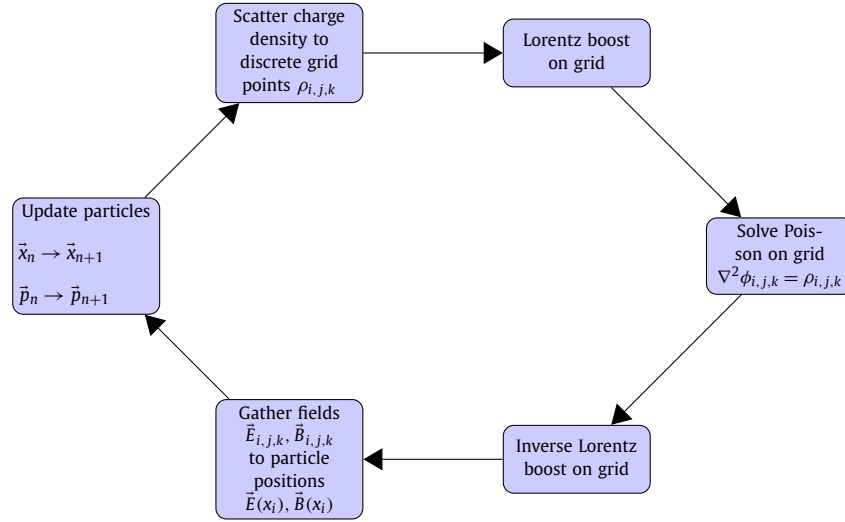


Fig. 1. Schematic of OPAL's static solver.

we explain the approach taken by OPAL-FEL's new full-wave solver (MITHRA).

The inhomogeneous Maxwell equations, with the Lorenz Gauge, are rearranged into two wave equations:

$$\begin{cases} \vec{\nabla} \cdot \vec{E} = \frac{\rho}{\epsilon_0}, \\ \vec{\nabla} \wedge \vec{E} = -\frac{\partial \vec{B}}{\partial t}, \\ \vec{\nabla} \cdot \vec{B} = 0, \\ \vec{\nabla} \wedge \vec{B} = \mu_0 \vec{j} + \frac{1}{c^2} \frac{\partial \vec{E}}{\partial t}, \end{cases} \Rightarrow \begin{cases} \nabla^2 \vec{A} - \frac{1}{c^2} \frac{\partial^2 \vec{A}}{\partial t^2} = -\mu_0 \vec{j}, \\ \nabla^2 \phi - \frac{1}{c^2} \frac{\partial^2 \phi}{\partial t^2} = -\frac{\rho}{\epsilon_0}, \end{cases} \quad (4)$$

where  $\vec{A}$  and  $\phi$  are the vector and scalar potentials respectively, related to the EM fields by

$$\begin{cases} \vec{E} = -\frac{\partial \vec{A}}{\partial t} - \vec{\nabla} \phi, \\ \vec{B} = \vec{\nabla} \wedge \vec{A}. \end{cases} \quad (5)$$

In the full-wave case we have hyperbolic PDEs (4), rather than the elliptic PDE that we had in the static case, thus the two solvers will use completely different methods. These wave equations and the equations of motion of the particles are coupled through the source terms  $\rho$  and  $\vec{j}$ , and through the Lorentz force that the fields exert on the particles

$$\vec{F} = q \left( \vec{E} + \vec{v} \wedge \vec{B} \right). \quad (6)$$

To solve these equations MITHRA uses a PIC scheme, similar to the static solver, in which the bunch is surrounded by a grid of points that contain the fields. However, here a finite difference time domain (FDTD [31]) method is used to integrate the fields, which means that at each time step both the particles and the fields on the grid are updated.

Unlike OPAL's static solver, which can stretch and rotate the grid as necessary to tightly enclose the bunch at each time step, FDTD requires the grid to be fixed in space because each grid-point is updated using its previous values, and thus it needs to enclose the whole domain where there will be EM fields of interest during the simulation. In the case of an undulator this means that the computational domain should have the same length as the undulator, usually within a range  $L_u \simeq 1\text{--}100$  m, but should also have a grid spacing small enough to resolve the bunch of length  $\sigma_z \simeq 0.1\text{--}1$  mm and the resonance frequency of the radiation  $\lambda_r \simeq 0.01\text{--}100$   $\mu\text{m}$ , which represents an order of  $\sim 10^6\text{--}10^{10}$  cells just for the longitudinal axis, extremely large even for the current state-of-the-art HPC clusters. In addition, FDTD algorithms

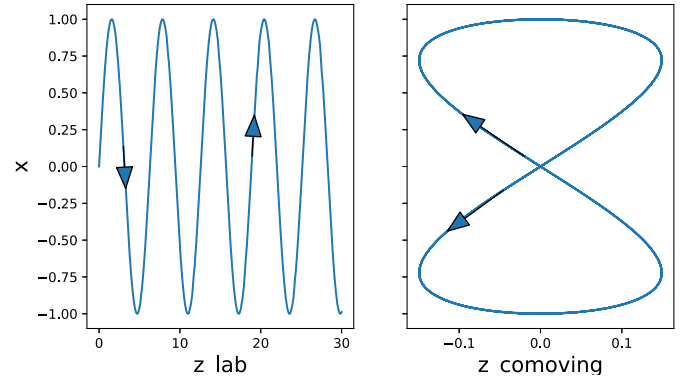


Fig. 2. Comparison between the particle trajectories in the laboratory (left) and the comoving frame (right). Particles are not static in the comoving frame, despite their average velocity being zero.

need to satisfy the Courant-Friedrichs-Lewy condition [32] to be stable, which sets an upper limit on the time-step  $\Delta t < \Delta z/c$ , and would imply also  $\sim 10^6\text{--}10^{10}$  steps for a single simulation.

MITHRA greatly reduces the computational cost of the simulation by doing the entire computation in a Lorentz-boosted frame at a constant speed, as suggested in [33,34]. In Fig. 2 we show the trajectory of the bunch in the lab and boosted frames. In the boosted frame the grid can be smaller and coarser, since the bunch's average velocity is zero, the undulator length is contracted, and the resonant wavelength is dilated. This is yet another difference with respect to the static solver: here the bunch and grid are boosted at the very start and end of the simulation only, and the particles are updated within the boosted frame. In contrast, the static solver boosts the grid at each time step, and the particles are always in the lab frame. While MITHRA's approach is beneficial from the computational point of view, it makes the RMS values of the bunch more difficult to interpret.

For parallelization, MITHRA divides the domain only along the longitudinal axis, and each processor contains an equal number of cells (see Fig. 3). This approach for load balancing makes sense for an FDTD solver where the grid is large and has many empty cells  $N_c \gg N_p$ , but will have the negative effect of having an unbalanced particle distribution, with few processors containing the majority of the particles. For more details on the algorithm, benchmarks, and examples, the reader is referred to the MITHRA manual [35].

In OPAL-FEL, the full-wave solver is a wrapper for MITHRA, which is initialized when the bunch enters a wiggler's fringe-field.

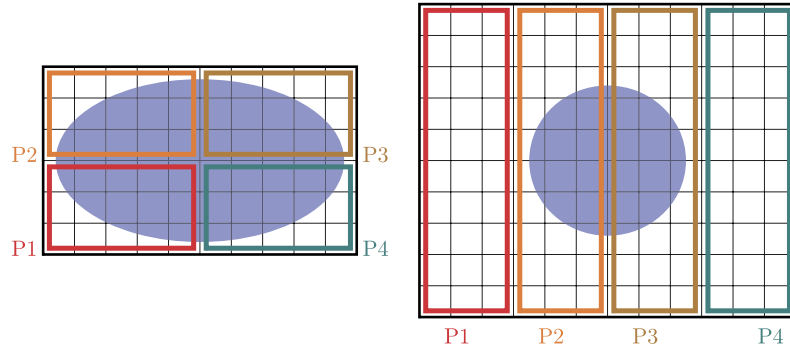


**Fig. 3.** Parallelization schemes used by OPAL's solvers. The blue ellipse is the bunch, and in this example four processors share the computational load. The static solver (left) adapts the grid to tightly surround the bunch, and equally shares the number of particles among processors. The full-wave solver MITHRA (right) cannot resize the grid, and equally shares the number of cells among processors. (For interpretation of the colours in the figure(s), the reader is referred to the web version of this article.)

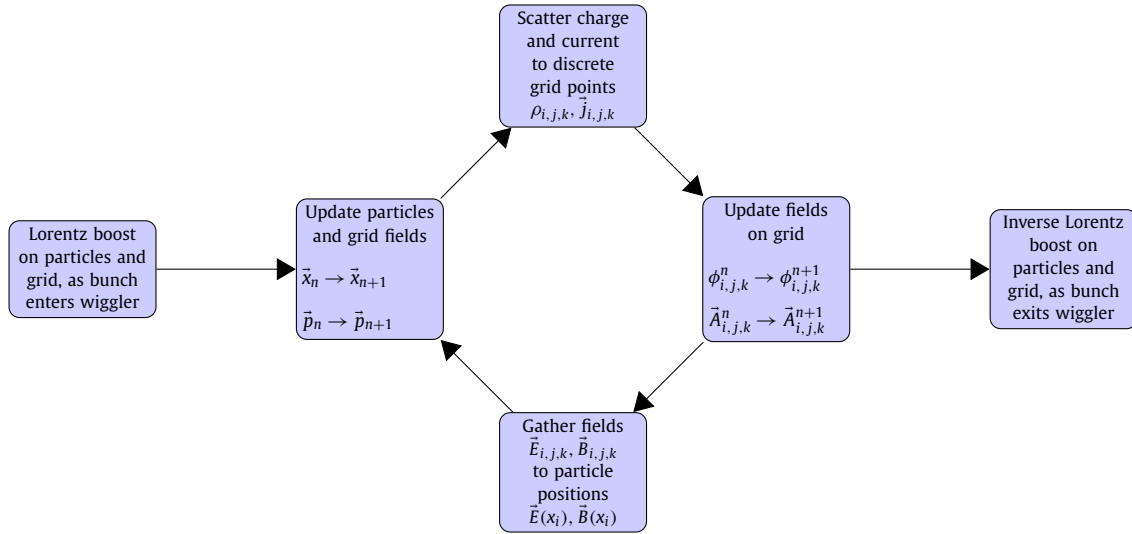


**Fig. 4.** Schematic of OPAL-FEL's full-wave solver.

At this point, the particles are Lorentz-boosted and remapped onto a new comoving grid. During the change of solver the particles completely redistributed among processors, due to the different parallelization schemes that the two solvers use. After this initial stage, the bunch is simulated traversing the full undulator or wiggler, just as in MITHRA. Once the bunch has completely exited the wiggler, OPAL-FEL does an inverse Lorentz boost on the particles, and changes back from the full-wave solver to static, again redistributing particles among processors and remapping them onto a smaller grid. (See Fig. 4.)

One drawback of OPAL-FEL that should be noted is the different computational requirements of the algorithms. As explained above, FDTD requires a much finer grid than the static solver, and hence requires more memory, and possibly more processors. Furthermore, a finer grid leads to less particles per cell, which will in turn lead to noise [36]. The noise can easily be reduced by increasing the number of particles, at the cost of increasing the memory requirement once again. These differences between solvers often require the user to run simulations with more particles and processors than would be necessary in the electrostatic sections of the beamline. Nevertheless, we have not found any examples where this drawback was computationally prohibitive.

As we will show in the remaining sections of the paper, this approach was successful at modeling a beamline with a wiggler, optimally combining the usage of the static solver in radiation free sections, with the full-wave solver in the wiggler.

### 3. LCLS benchmark

Wigglers and undulators can be used in FELs, not only at the end of the linac to produce coherent radiation, but also in the upstream section of the linac to reshape the electron bunch phase space. In these cases, a wiggler and a laser pulse are overlapped to generate small energy modulations in the bunch, that can later be compressed into short bunches [37,38].

In [13], MacArthur et al. investigate the possibility to generate a single cycle energy modulation in an electron bunch by means of a wiggler, but without the aid of an external laser. Using a line charge model they argue that a long bunch with a high-charge tail (Fig. 5), should emit coherent radiation strong enough to imprint an energy modulation in the beam core. In the paper they also validate their hypothesis through computer simulations with the electromagnetic code Osiris [23], and with an experiment at LCLS.

The same experiment was simulated in OPAL-FEL to serve as a benchmark, as it represents an example where both space charge and radiation effects are important, and thus the full Maxwell equations need to be considered. The model included the 2.10 m wiggler, and an 80 cm drift before and after it, such that the initial and final bunch positions would be clear from the fringe fields. The input bunch had a charge of  $Q = 200$  pC, a transverse rms size  $\sigma_{x,y} = 74$   $\mu\text{m}$ , an average energy of  $E = 3.95$  GeV with an energy spread of  $\sigma_E = 2$  MeV, and a current profile as shown in Fig. 5. The wiggler had a strength parameter  $K = 51.5$ , and 6 periods of length  $\lambda_w = 35$  cm.



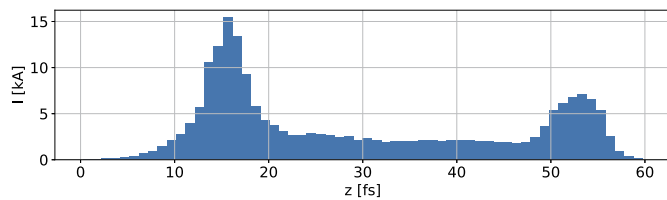


Fig. 5. Initial bunch current for the LCLS simulation.

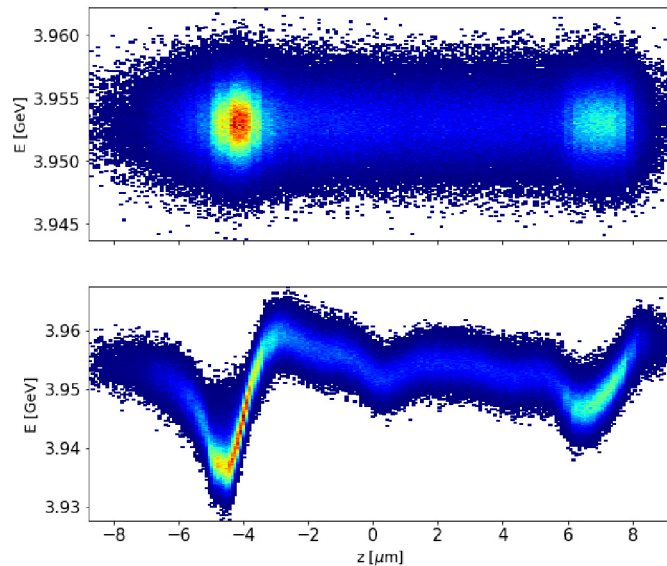


Fig. 6. Longitudinal phase space of the electron bunch in the LCLS OPAL-FEL simulation (top) before the wiggler, at the starting point of the simulation, and (bottom) after the wiggler, where the phase space has been reshaped by wiggler-induced radiation.

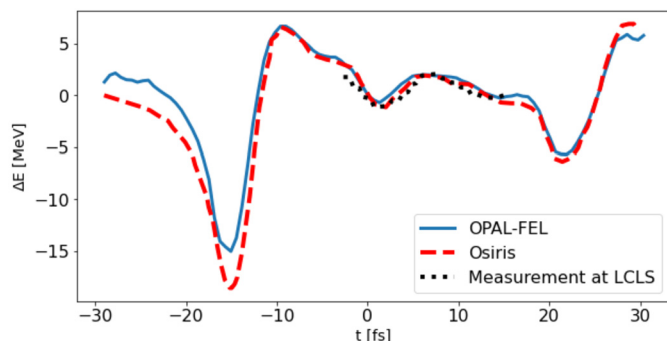


Fig. 7. Comparison of the final slice-averaged energy between the OPAL-FEL simulation, and the OSIRIS simulation and measurement by MacArthur et al. [13].

The longitudinal phase space before and after the wiggler can be seen in Fig. 6, where the wiggler-induced effects are clearly visible. The wake fields inside the wiggler affect mostly the high-charge spikes in the head and tail of the bunch. Less noticeably, the radiation also causes a chirp in the bunch center, as predicted by the theory. In Fig. 7 we see the slice-energy, where the single cycle energy modulation in the bunch center is evident. The slice-energy is also plotted for the OSIRIS simulation and the measurement at LCLS carried out by MacArthur et al. OPAL-FEL simulations closely follow these results.

## 4. AWA experiment and benchmark

### 4.1. Experimental setup

Among several available AWA beamlines [39,40], the straight section after the linac was used for this experiment (see Fig. 8). The first 13 meters of the beamline form the photoinjector, consisting of a photocathode gun and six accelerating cavities. During this experiment, 4 accelerating cavities were used to generate 300 pC electron bunches with energy of 45.6 MeV. The straight section of the beamline that follows after the photoinjector is referred to as the “experimental beamline”. It includes four matching quadrupoles (Q1-Q4, referred to as upstream quadrupoles), a wiggler, a longitudinal phase space (LPS) measurement section, and several YAG screens (diagnostic stations equipped with 50-mm diameter Cerium-doped Yttrium aluminium garnet (Ce:YAG or YAG for short) electron imaging screens to measure the transverse beam distribution) (Fig. 8). The upstream quadrupoles are used to match the beam from the photoinjector to produce the required transverse beam conditions at the wiggler center. The wiggler can be mechanically inserted in and out of the experimental beamline such that we were able to insert or remove the wiggler from the beam path (referred to as wiggler-in and wiggler-out settings). The LPS measurement section at the end of the beamline is used to measure the beam’s temporal and energy spectrum perturbations after having passed through the wiggler. The LPS consists of four more quadrupole magnets (Q5-Q8, referred to as downstream quadrupoles) for transverse focusing at YAG5 and YAG6, a 100 μm horizontal slit for improved temporal resolution, a transverse deflecting cavity (TDC) and an energy spectrometer. The slit can be inserted or removed from the beamline when necessary.

The AWA photoinjector was used to generate a 300 pC electron bunch with an rms bunch length of around 0.1 mm. The photoinjector parameters to achieve this were determined with OPAL-t numerical simulations. The laser spot size (diameter) on the cathode was 12 mm and its pulse length (FWHM) was 300 fs. A single solenoid, located at the photocathode gun exit, was used to match bunches into the linac and on to the upstream quadrupoles. The solenoid was used to create a transverse waist at the entrance to the upstream quadrupole (i.e. Q1). The upstream quadrupoles were then easily used to match to the transverse beam conditions needed at the center of the wiggler.

The measurement of the Twiss parameters at the wiggler center with wiggler-out was necessary for this experiment. However, the experimental beamline does not allow for the installation of a YAG screen at that point. For this reason we used a three screen method instead [41], to measure the Twiss parameters. Once the upstream quadrupoles had been set to produce a specific beam condition, the three YAG screens (YAG1, YAG2, and YAG3), which are separated by drifts, were used to measure the rms beam sizes. We then analytically fit the beam sizes at the YAGs (wiggler-out), to obtain the Twiss parameters at YAG1 and at the wiggler center.

The main measurement necessary for this experiment was that of the longitudinal phase space. Since we know that the wiggler perturbs the beam’s temporal and energy spectrums, we needed to compare the LPS of the wiggler-in to the LPS of the wiggler-out (and to our simulations). Downstream of the wiggler, the beam passes through the four downstream quadrupoles which are used to minimize transverse contributions on YAG5 and YAG6 [42], where the longitudinal measurements are made. The 100 μm horizontal slit can be used in some cases to truncate the beam vertically to improve temporal resolution. The TDC deflects the beam in the vertical direction such that the temporal information gets projected onto the YAG in vertical direction. Energy spectrum information appears on the YAG in horizontal direction because the 20 degree energy spectrometer horizontally bends the beam de-

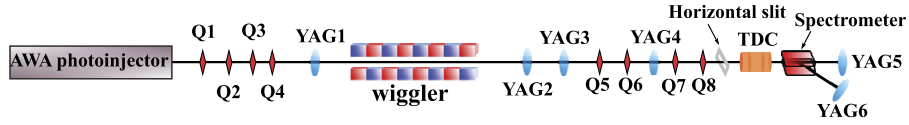


**Fig. 8.** Experimental beamline at AWA. Note that the wiggler and slit can be inserted or removed from the beamline when required. The shown configuration is the wiggler-in case; in the wiggler-out case a simple drift replaces the wiggler.

**Table 1**  
Beam size at the center of the wiggler for the two beam settings.

	$\sigma_x$ [mm]	$\sigma_y$ [mm]
Round Beam	0.4	0.4
Elliptic Beam	2.5	0.4

pending on electron's energy. The LPS measurement section is able to measure the temporal distribution and the energy spectrum and the LPS, separately or simultaneously. In the case of temporal distribution only measurement (TDC-only), we focused the beam vertically at YAG5 and turned on the TDC (without the slit). Similarly, the energy spectrum (spectrometer-only) was measured with horizontal beam focusing at YAG6 with the energy spectrometer turned on (also without the slit). Lastly, the LPS measurement required transverse beam focusing at YAG5, the horizontal slit, and turning on both the TDC and the energy spectrometer. Note that drift length from the spectrometer to YAG5 and to YAG6 is the same.

The experiments and measurements were carried out for two specific settings of the upstream quadrupoles. They were set such that the transverse beam size would have a waist at the center of the wiggler. The two settings are from here on referred to as *round beam* and *elliptic beam*, and only differ in their transverse size, described in Table 1.

The choice of the two transverse beam sizes was made in an attempt to perform an experiment that probed both above and below the wiggler's radiation diffraction limit  $\sigma_{diff}$ , given by

$$\sigma_{diff} = \sqrt{\sigma_z \frac{\lambda_w}{2\pi}}, \quad (7)$$

where  $\sigma_z$  is the longitudinal rms size of the bunch, and  $\lambda_w$  the wiggler period. From [14] we expect that with a transverse beam size  $\sigma_r \gg \sigma_{diff}$  the wiggler-induced radiation effects become negligible, and only the space charge effects remain. In the current experiment, with an average bunch length of  $\sigma_z = (250 \pm 40) \mu\text{m}$  and a wiggler period  $\lambda_w = 8.5 \text{ cm}$ , we find  $\sigma_{diff} = (1.84 \pm .15) \text{ mm}$ . For this reason the horizontal beam size  $\sigma_x$  was chosen to be in one case greater and in one case smaller than  $\sigma_{diff}$ . The vertical beam size  $\sigma_y$  was unfortunately limited by the height of the vacuum chamber in the wiggler, and thus remained below the diffraction limit at all times.

#### 4.2. OPAL-FEL benchmark

In order to benchmark OPAL-FEL with the AWA wiggler experiment, the experimental beamline was computationally modeled and used for simulations that could be compared to the experiment. The simulated section goes from the first electron imaging screen (YAG1) up to the energy spectrometer 7 meters downstream. This section includes the wiggler, four YAGs for transverse beam measurements, the four downstream quadrupoles, and the LPS measurement section (Fig. 8).

Simulating the electron bunch starting from YAG1, requires accurate knowledge of the bunch parameters in all 3 phase space planes at YAG1. The transverse beam parameters were known, since the transverse emittance and Twiss parameters at YAG1 were

**Table 2**  
Twiss parameters at YAG1 as measured during the experiment.

	$\beta_x$ [m]	$\alpha_x$ [ ]	$\epsilon_x$ [ $\mu\text{m}$ ]	$\beta_y$ [m]	$\alpha_y$ [ ]	$\epsilon_y$ [ $\mu\text{m}$ ]
Round beam	3.83	-1.74	34.1	4.37	-1.19	14.4
Elliptic beam	20.0	-0.23	31.7	2.84	-0.93	17.1

measured by the three-screen methods using YAG1-3. These transverse beam parameters can be seen in Table 2.

The longitudinal beam parameters were numerically recreated at YAG1 by the following method. The LPS was not directly known at YAG1, as it was only measured at the LPS measurement section at the end of the beamline. There, the spectrometer and TDC provided images of the longitudinal particle distribution and the energy spread, of which examples can be seen in Fig. 9. These images are available for both the round and elliptic beam experiments. Additionally, in each case, the experiment and images were repeated with the wiggler in the beamline (wiggler-in), and the wiggler removed from the beamline (wiggler-out). The images from the wiggler-in experiments were used later on for benchmarking the simulations, while the wiggler-out images were used to numerically recreate the LPS at YAG1. In this way, the longitudinal parameters at YAG1 were combined with the Twiss parameters at YAG1 to obtain the initial bunch conditions for the simulations.

In summary, the following steps were carried out to recover the full 6D phase space at YAG1:

1. A 2D particle distribution was generated with the energy spread from the spectrometer images (Fig. 9b), and with the longitudinal distribution from the TDC images (Fig. 9c). The correlation of this 2D distribution was taken from the  $z-E$  correlation seen in the LPS images (Fig. 9a), which were captured with both the spectrometer and TDC simultaneously turned on. The resulting 2D distribution was the LPS at the spectrometer (Fig. 9d). All the images used in this step were taken with the wiggler-out. Note that the energy spectrum from the spectrometer shows a "bump" at 45.6 MeV of energy (Fig. 9b). The source of this anomaly was discovered to be a low charge satellite bunch that was spuriously emitted from the cathode. This satellite bunch trailed the main bunch 4.5 mm behind it, and had a charge of approximately 6 pC. The effect of this low charge bunch is negligible with respect to the 300 pC main bunch, and was thus not included in the simulations.
2. The Twiss parameters at the spectrometer were computed by transferring the Twiss parameters from YAG1 (Table 2), through the 7 meter section of the beamline to the spectrometer in the wiggler-out case, using linear transfer matrices.
3. With the known Twiss parameters at the spectrometer, it was possible to sample the 4D transverse phase-space, and add it to the 2D longitudinal phase space generated in step 1, giving us the full 6D particle distribution. Note that with this method there were assumed to be no longitudinal-transverse correlations in the bunch.
4. Finally, since OPAL's electrostatic solver assumes conservative forces, the simulation can be run in reverse to effectively track the bunch back in time. Using this approach, the bunch was simulated backwards from the spectrometer to YAG1, with the wiggler-out, thus obtaining the 6D particle distribution at YAG1 (Fig. 10), the starting point of our simulations.

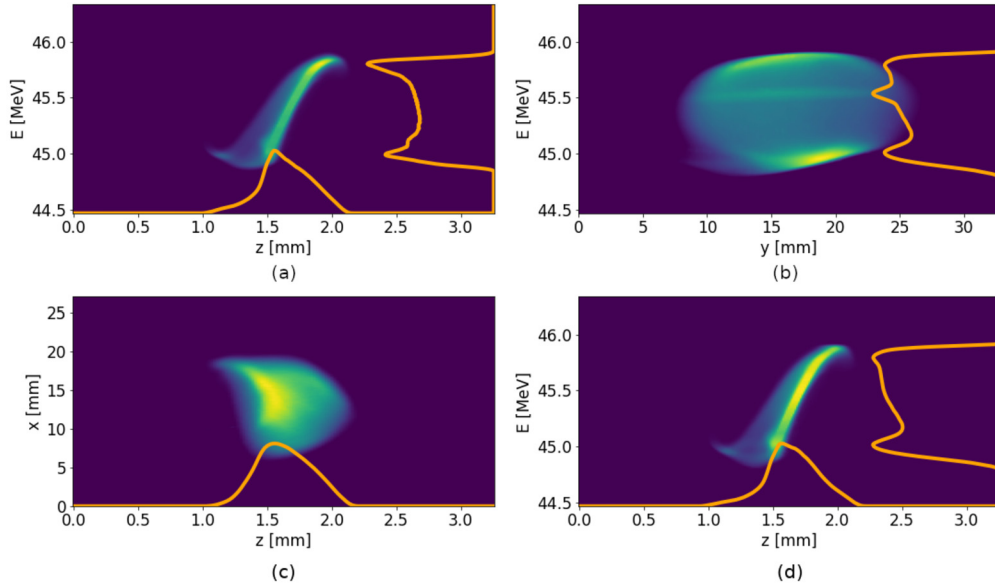


**Fig. 9.** (a to c) Experimental YAG images taken with the wiggler out of the beamline, in the case of the round beam. All images show a bunch with charge  $Q = (300 \pm 4)$  pC. (a) LPS observed on YAG6 with the TDC and spectrometer turned on. For this image a horizontal slit was placed in front of the TDC. (b) Energy distribution of the beam observed on YAG6, obtained with the spectrometer turned on. (c) Longitudinal particle distribution observed on YAG5 with the TDC turned on. (d) Numerical particle distribution generated by combining images a, b and c, which was used for the back-tracking simulations.

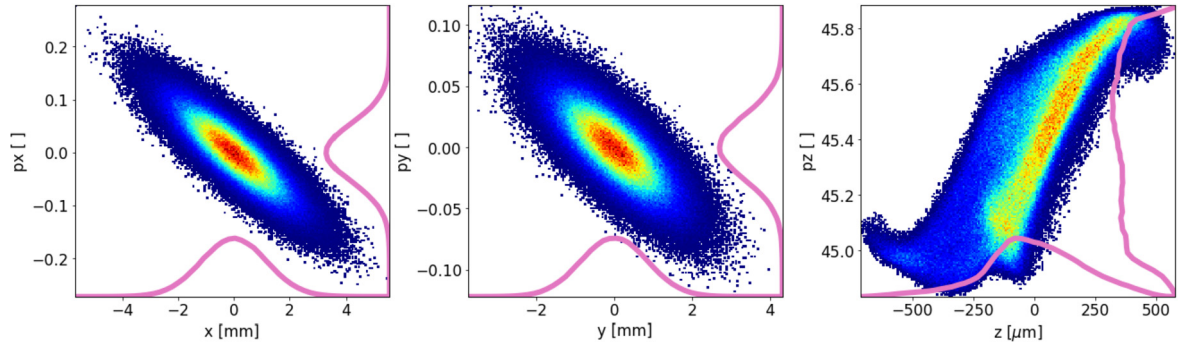


**Fig. 10.** Initial particle distribution for the simulations of the round beam. This is the bunch's 6D phase space at YAG1.

With these four steps we were able to obtain the initial bunch conditions which were needed for our wiggler-in simulations.

Note that simulation back-tracking only works in the wiggler-out case, because only the electrostatic solver can be run in reversed time. The MITHRA solver that OPAL-FEL uses to track the bunch through a wiggler cannot be run backwards in time.

The reader might remark that the experimental shots that combined the TDC and spectrometer simultaneously (Fig. 9a) provide a full picture of the LPS, and these LPS images could have been used to generate the 2D longitudinal particle distribution, instead of combining the TDC-only and spectrometer-only shots as we did. However, the shot from Fig. 9a was captured with a horizontal slit present in the beamline, placed in front of the TDC (Fig. 8). This slit blocked part of the bunch, potentially distorting the histograms. As a consequence, we only took the  $z - E$  correlation from these images, but not the energy and  $z$  histograms. In the TDC-only and spectrometer-only images (Figs. 9b and c), the slit was not present, thus all electrons reached the YAG screens.

With the known full particle distribution at YAG1, forward-time simulations were carried out with the bunch going through the wiggler and up to the spectrometer. The final LPS from the simulations can be compared to the experimental wiggler-in LPS shots (Figs. 11, 12).

The most notable effect that the wiggler has on the bunch, as can be seen by comparing the wiggler-out and wiggler-in shots,

**Table 3**

Values for the FWHM of the energy histograms observed on YAG6, from simulations and experiments.

	FWHM <sub>E</sub> [MeV]
Round beam, wiggler-out, exp	$1.01 \pm 0.03$
Round beam, wiggler-in, exp	$1.24 \pm 0.03$
Round beam, wiggler-in, sim	$1.22 \pm 0.04$
Elliptic beam, wiggler-out, exp	$0.91 \pm 0.03$
Elliptic beam, wiggler-in, exp	$1.08 \pm 0.03$
Elliptic beam, wiggler-in, sim	$1.03 \pm 0.04$

is an increase in the total energy spread. This effect was to be expected since, as explained in the introduction 1, the wiggler increases the plasma oscillation frequency of the bunch by enhancing space charge [15]. The same effect is also observed in simulations, as is apparent from the plots and Table 3, where the full-width at half-maximum (FWHMs) of the energy spreads are reported.

Experiments and simulations closely agree with respect to the increase in energy spread in presence of the wiggler. However, some discrepancies in the shape of the phase space distribution can be seen, most notably between Figs. 12 b and c. These differences are suspected to be due to inaccuracies in the bunch's initial conditions for the simulations, and in the experimental phase space images. Indeed, as explained above, the phase space im-

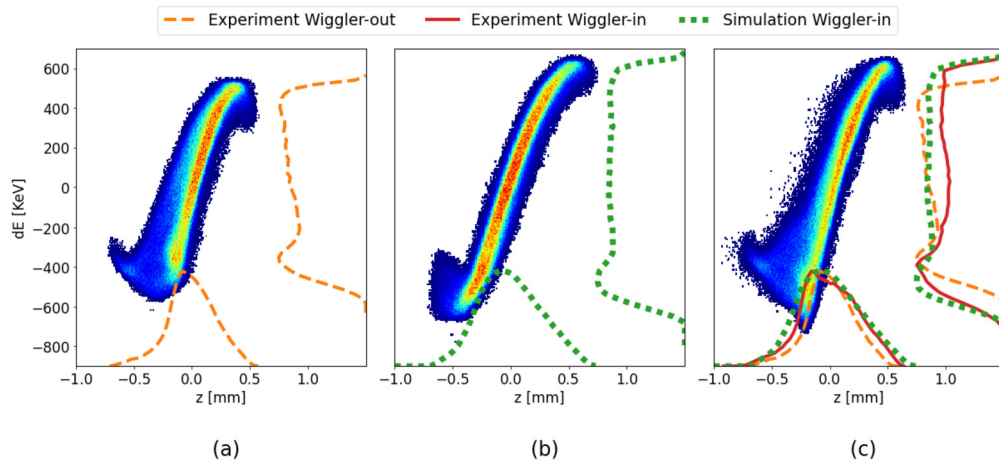


**Fig. 11.** LPS of the round beam, at YAG6 in the (a) wiggler-out experiment, (b) the wiggler-in experiment, and (c) the simulation with wiggler-in. The experimental images (a) and (b) were obtained by combining three YAG shots, as explained in Fig. 9.

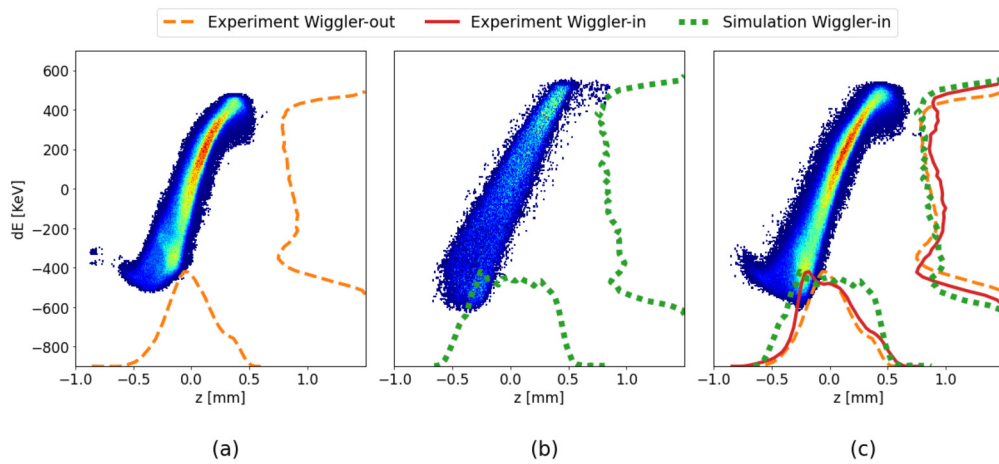


**Fig. 12.** LPS of the elliptic beam, at YAG6 in the (a) wiggler-out experiment, (b) the wiggler-in experiment, and (c) the simulation with wiggler-in. The experimental images (a) and (b) were obtained by combining three YAG shots, as explained in Fig. 9.

ages and initial conditions for the simulations were obtained by combining several experimental shots and measurements, thus not allowing for an entirely realistic modeling of the bunch.

## 5. Conclusion and further work

Good agreement with the experimental results has been demonstrated in the modeling of two experiments using OPAL-FEL. The considered experiments allowed us to test the code in different regimes of electron-wiggler interaction: a higher-energy case (cf. section 3) governed by the effects of emitted radiation, and a lower-energy case (cf. section 4) governed by space charge effects. We have now all reasons to believe that the code can be reliably used for modeling of complex beamlines consisting of magnetic chicanes, wigglers, and undulators simultaneously accounting for the space charge and coherent synchrotron radiation effects.

With the OPAL-FEL code and thanks to the parallel nature of OPAL, full start-to-end modeling of complex beamlines is possible. In regions where radiation does not play a significant role, the 3D electrostatic solver is used, while in undulators and wigglers the full 3D electromagnetic solver will take radiation into account. The ability of OPAL-FEL to switch between the two solvers reduces the computational expense of simulations by using the faster electrostatic solver in the sections where radiation can be neglected. Adapting the numerical model to the physics needs has a great

positive impact on the time to solution and contributes to an economical use of computing resources.

The current plan is to apply OPAL-FEL to evaluate the gain in the recently proposed wiggler enhanced plasma cascade amplifier [43] for coherent electron cooling [44]. It is expected to be particularly fruitful since both the space charge and coherent synchrotron radiation effects are considered to play equally important roles there.

## CRedit authorship contribution statement

**Arnau Albà** integrated OPAL and MITHRA, carried out simulations, analyzed the experimental data and led preparation of the paper for a publication; **Jimin Seok** conducted the experiment, analyzed the data and contributed to paper writing; **Andreas Adelman** provided ideas for OPAL-FEL, provided the oversight for the data analysis, and contributed to paper writing; **Gwanghui Ha** conducted the experiment; **Soonhong Lee, Maofei Qian, and Joseph Xu** designed the wiggler and provided the oversight for a fabrication of the wiggler's strong back; **Yinghu Piao** carried out magnetic measurements and wiggler's tuning; **Scott Doran** designed the wiggler's vacuum chamber and support, installed the wiggler, and assembled the beamline; **Eric Wisniewski** assembled the beamline; **John Power** provided the oversight for the experiment and data analysis; **Alexander Zholents** conceived the experiment, led the activity and contributed to paper writing.



## Declaration of competing interest

The authors declare that they have no known competing financial interests or personal relationships that could have appeared to influence the work reported in this paper.

## Data availability

Data will be made available on request.

## Acknowledgements

We are grateful to John TerHAAR, Joseph Gagliano III, and Eric McCarthy from the Advanced Photon Source of Argonne National Laboratory who assembled the wiggler that worked flawlessly in the experiment. This work was supported by FY 2018 Research and Development for Next Generation Nuclear Physics Accelerator Facilities DOE National Laboratory Announcement Number: LAB 18-184 Proposal ID 0000235339.

## References

- [1] H. Winick, G. Brown, K. Halbach, J. Harris, *Phys. Today* 34 (5) (1981) 50–63, <https://doi.org/10.1063/1.2914568>.
- [2] G.N. Kulipanov, *Phys. Usp.* 50 (4) (2007) 368–376, <https://doi.org/10.1070/PU2007v050n04ABEH006237>, <http://mi.mathnet.ru/ufn454>.
- [3] J.A. Clarke, *The Science and Technology of Undulators and Wigglers*, Oxford University Press, 2004.
- [4] G. Stupakov, S. Heifets, *Phys. Rev. Spec. Top., Accel. Beams* 5 (2002) 054402, <https://doi.org/10.1103/PhysRevSTAB.5.054402>, <https://link.aps.org/doi/10.1103/PhysRevSTAB.5.054402>.
- [5] J.M. Byrd, W.P. Leemans, A. Loftsdottir, B. Marcellis, M.C. Martin, W.R. McKinney, F. Sannibale, T. Scarvie, C. Steier, *Phys. Rev. Lett.* 89 (2002) 224801, <https://doi.org/10.1103/PhysRevLett.89.224801>, <https://link.aps.org/doi/10.1103/PhysRevLett.89.224801>.
- [6] M. Abo-Bakr, J. Feikes, K. Holldack, G. Wüstefeld, H.-W. Hübers, *Phys. Rev. Lett.* 88 (2002) 254801, <https://doi.org/10.1103/PhysRevLett.88.254801>, <https://link.aps.org/doi/10.1103/PhysRevLett.88.254801>.
- [7] U. Arp, G.T. Fraser, A.R. Hight Walker, T.B. Lucatorto, K.K. Lehmann, K. Harkay, N. Sereno, K.-J. Kim, *Phys. Rev. Spec. Top., Accel. Beams* 4 (2001) 054401, <https://doi.org/10.1103/PhysRevSTAB.4.054401>, <https://link.aps.org/doi/10.1103/PhysRevSTAB.4.054401>.
- [8] G.L. Carr, M.C. Martin, W.R. McKinney, K. Jordan, G.R. Neil, G.P. Williams, *Nature* 420 (2002) 153–156, <https://doi.org/10.1038/nature01175>.
- [9] B. Podobedov, G. Carr, S. Kramer, J. Murphy, in: *Proceedings of the 2001 IEEE Particle Accelerator Conference*, Chicago, IL, 2002, p. 1921.
- [10] J. Wu, T. Raubenheimer, G. Stupakov, *Phys. Rev. Spec. Top., Accel. Beams* 6 (2003) 040701.
- [11] A.A. Zholents, *Phys. Rev. Spec. Top., Accel. Beams* 8 (2005) 040701, <https://doi.org/10.1103/PhysRevSTAB.8.040701>, <https://link.aps.org/doi/10.1103/PhysRevSTAB.8.040701>.
- [12] J.P. Duris, J.P. MacArthur, J.M. Glowina, S. Li, S. Vetter, A. Miahnahri, R. Coffee, P. Hering, A. Fry, M.E. Welch, A. Lutman, F.-J. Decker, D. Böhler, J.A. Mock, C. Xu, K. Gumerlock, J.E. May, A. Cedillos, E. Kraft, M.A. Carrasco, B.E. Smith, L.R. Chieffo, J.Z. Xu, J.P. Cryan, Z. Huang, A. Zholents, A. Marinelli, *Phys. Rev. Lett.* 126 (2021) 104802, <https://doi.org/10.1103/PhysRevLett.126.104802>, <https://link.aps.org/doi/10.1103/PhysRevLett.126.104802>.
- [13] J.P. MacArthur, J. Duris, Z. Zhang, A. Lutman, A. Zholents, X. Xu, Z. Huang, A. Marinelli, *Phys. Rev. Lett.* 123 (2019) 214801, <https://doi.org/10.1103/PhysRevLett.123.214801>, <https://link.aps.org/doi/10.1103/PhysRevLett.123.214801>.
- [14] G. Geloni, E. Saldin, E. Schneidmiller, M. Yurkov, *Nucl. Instrum. Methods Phys. Res., Sect. A, Accel. Spectrom. Detect. Assoc. Equip.* 583 (2) (2007) 228–247, <https://doi.org/10.1016/j.nima.2007.09.019>, <https://www.sciencedirect.com/science/article/pii/S0168900207020001>.
- [15] G. Geloni, E. Saldin, E. Schneidmiller, M. Yurkov, *Nucl. Instrum. Methods Phys. Res., Sect. A, Accel. Spectrom. Detect. Assoc. Equip.* 554 (1) (2005) 20–48, <https://doi.org/10.1016/j.nima.2005.07.057>, <https://www.sciencedirect.com/science/article/pii/S0168900205015305>.
- [16] D. Ratner, *Phys. Rev. Lett.* 111 (2013) 084802, <https://doi.org/10.1103/PhysRevLett.111.084802>, <https://link.aps.org/doi/10.1103/PhysRevLett.111.084802>.
- [17] G. Stupakov, P. Baxevanis, *Phys. Rev. Spec. Top., Accel. Beams* 22 (2019) 034401, <https://doi.org/10.1103/PhysRevAccelBeams.22.034401>, <https://link.aps.org/doi/10.1103/PhysRevAccelBeams.22.034401>.
- [18] G. Stupakov, J. Tang, *Phys. Rev. Spec. Top., Accel. Beams* 24 (2021) 020701, <https://doi.org/10.1103/PhysRevAccelBeams.24.020701>, <https://link.aps.org/doi/10.1103/PhysRevAccelBeams.24.020701>.
- [19] S.G. Biedron, H.P. Freund, S.V. Milton, 3d Fel Code for the Simulation of a High-Gain Harmonic Generation Experiment, *Free-Electron Laser Challenges II*, vol. 3614, International Society for Optics and Photonics, 1999, pp. 96–108.
- [20] S. Reiche, et al., in: *Proceedings of the 2014 FEL Conference*, 2014, pp. 403–407.
- [21] H. Freund, P. van der Slot, et al., in: *Proceedings of the 36th International Free Electron Laser Conference*, 2014, pp. 408–411.
- [22] A. Fallahi, A. Yahaghi, F.X. Kärtner, *Comput. Phys. Commun.* 228 (2018) 192–208, <https://doi.org/10.1016/j.cpc.2018.03.011>, <https://www.sciencedirect.com/science/article/pii/S0010465518300833>.
- [23] R.A. Fonseca, et al., in: *Proceedings of the International Conference on Computational Science-Part III*, 2002, pp. 342–351.
- [24] A. Albà, A. Adelman, A. Fallahi, in: *33rd International Vacuum Nanoelectronics Conference (IVNC 2020)* (Virtual), Lyon, France, July 6–10, 2020, IEEE, Piscataway, NJ, 2020, p. 9203404, Due to the Coronavirus (Covid-19) the conference was conducted virtually, <https://doi.org/10.1109/IVNC49440.2020.9203404>.
- [25] A. Adelman, et al., *OPAL a versatile tool for charged particle accelerator simulations*, arXiv:1905.06654, 2019.
- [26] R.W. Hockney, J.W. Eastwood, *Computer Simulation Using Particles*, Hilger, Bristol, 1988.
- [27] J.P. Boris, in: *Proceedings of Fourth Conference on Numerical Simulations of Plasmas*, 1970.
- [28] J. Qiang, S. Lidia, R.D. Ryne, C. Limborg-Deprey, *Phys. Rev. Spec. Top., Accel. Beams* 9 (4) (2006) 044204, <https://doi.org/10.1103/PhysRevSTAB.9.044204>, <https://link.aps.org/doi/10.1103/PhysRevSTAB.9.044204>.
- [29] K. Floettmann, *Astra Manual*, [https://www.desy.de/~mpyflo/Astra\\_manual/Astra-Manual\\_V3.2.pdf](https://www.desy.de/~mpyflo/Astra_manual/Astra-Manual_V3.2.pdf), Mar. 2017.
- [30] J.D. Jackson, *Classical Electrodynamics*, John Wiley & Sons, 1962.
- [31] B. Archambeault, O.M. Ramahi, C. Brench, *EMI/EMC Computational Modeling Handbook*, Springer, Boston, MA, 1998, chapter: The Finite-Difference Time-Domain Method.
- [32] R. Courant, K. Friedrichs, H. Lewy, *IBM J. 1* (2) (1967) 215–234.
- [33] W.F. amd, J.-L. Vay, *AIP Conf. Proc.* 1086 (2009) 346.
- [34] J.-L. Vay, Noninvariance of space- and time-scale ranges under Lorentz transformation and the implications for the study of relativistic interactions, *Phys. Rev. Lett.* 98 (2007) 130405.
- [35] A. Fallahi, MITHRA 2.0, a full-wave simulation tool for free electron lasers, <https://github.com/aryafallahi/mithra>. (Accessed 15 May 2020).
- [36] C.K. Birdsall, A.B. Langdon, *Plasma Physics via Computer Simulation*, CRC Press, 2004.
- [37] A.A. Zholents, G. Penn, *Phys. Rev. Spec. Top., Accel. Beams* 8 (5) (2005) 050704, <https://doi.org/10.1103/PhysRevSTAB.8.050704>, <https://link.aps.org/doi/10.1103/PhysRevSTAB.8.050704>.
- [38] E. Hemsing, G. Stupakov, D. Xiang, A. Zholents, *Rev. Mod. Phys.* 86 (3) (2014) 897–941, <https://doi.org/10.1103/RevModPhys.86.897>, <https://link.aps.org/doi/10.1103/RevModPhys.86.897>.
- [39] M. Conde, S. Antipov, D. Doran, W. Gai, Q. Gao, G. Ha, C. Jing, W. Liu, N. Neveu, J. Power, et al., in: *Proc. IPAC'17*, 2017, pp. 2885–2887.
- [40] G. Ha, J.G. Power, M. Conde, D.S. Doran, W. Gai, Limiting effects in double eex beamline, *J. Phys. Conf. Ser.* 874 (2017) 012061.
- [41] A. Wolski, D.C. Christie, B.L. Milityn, D.J. Scott, H. Kockelbergh, *Phys. Rev. Spec. Top., Accel. Beams* 23 (2020) 032804, <https://doi.org/10.1103/PhysRevAccelBeams.23.032804>, <https://link.aps.org/doi/10.1103/PhysRevAccelBeams.23.032804>.
- [42] Q. Gao, J. Shi, H. Chen, G. Ha, J.G. Power, M. Conde, W. Gai, *Phys. Rev. Spec. Top., Accel. Beams* 21 (2018) 062801, <https://doi.org/10.1103/PhysRevAccelBeams.21.062801>, <https://link.aps.org/doi/10.1103/PhysRevAccelBeams.21.062801>.
- [43] G. Stupakov, A. Zholents, in: *Proceedings of the Workshop Cool 2021, Novosibirsk*, 2021, <https://doi.org/10.18429/JACoW-COOL2021-S803>, in press.
- [44] V.N. Litvinenko, Y.S. Derbenev, *Phys. Rev. Lett.* 102 (2009) 114801, <https://doi.org/10.1103/PhysRevLett.102.114801>, <https://link.aps.org/doi/10.1103/PhysRevLett.102.114801>.